2862–2876 *Nucleic Acids Research, 2023, Vol. 51, No. 6* *Published online 2 March 2023*
https://doi.org/10.1093/nar/gkad082

Near-physiological *in vitro* assembly of 50S ribosomes involves parallel pathways

Xiyu Dong[1,†], Lili K. Doerfel[1,†], Kai Sheng[1], Jessica N. Rabuck-Gibbons[1,2], Anna M. Popova[1], Dmitry Lyumkis[1,2,3] and James R. Williamson[1,*]

[1]Department of Integrative Structural and Computational Biology, Department of Chemistry, and The Skaggs Institute for Chemical Biology, The Scripps Research Institute, La Jolla, CA 92037, USA, [2]Laboratory of Genetics, The Salk Institute for Biological Studies, La Jolla, CA 92037, USA and [3]Graduate School of Biological Sciences, Section of Molecular Biology, University of California San Diego, La Jolla, CA 92093, USA

Received November 23, 2022; Revised January 17, 2023; Editorial Decision January 19, 2023; Accepted February 25, 2023

ABSTRACT

Understanding the assembly principles of biological macromolecular complexes remains a significant challenge, due to the complexity of the systems and the difficulties in developing experimental approaches. As a ribonucleoprotein complex, the ribosome serves as a model system for the profiling of macromolecular complex assembly. In this work, we report an ensemble of large ribosomal subunit intermediate structures that accumulate during synthesis in a near-physiological and co-transcriptional *in vitro* reconstitution system. Thirteen pre-50S intermediate maps covering the entire assembly process were resolved using cryo-EM single-particle analysis and heterogeneous subclassification. Segmentation of the set of density maps reveals that the 50S ribosome intermediates assemble based on fourteen cooperative assembly blocks, including the smallest assembly core reported to date, which is composed of a 600-nucleotide-long folded rRNA and three ribosomal proteins. The cooperative blocks assemble onto the assembly core following defined dependencies, revealing the parallel pathways at both early and late assembly stages of the 50S subunit.

INTRODUCTION

The ribosome is one of the largest and most complicated enzymes in cells and is responsible for protein synthesis in all organisms on earth. The bacterial ribosome makes up 25% of the cell's dry mass (1), has a total mass of ∼2.5 MDa, and is composed of 3 ribosomal RNAs and 54 ribosomal proteins. The process by which ribosomal components interact with each other and assemble into functional ribosomes is termed ribosome biogenesis. During bacterial ribosome biogenesis, the primary transcript is cleaved into three ribosomal RNAs. The rRNAs fold into secondary and tertiary structures and bind with the ribosomal proteins, chaperoned by dozens of ribosome biogenesis factors, including rRNA modification enzymes (2–4). Despite its complexity, the process of bacterial ribosome assembly takes ∼2 min in cells (5,6), so the intermediates during the step-wise assembly process are short-lived and are present at ∼2% of the entire ribosome population in rapidly growing bacterial cells (6). Thus, it is difficult to directly separate and investigate the ribosome assembly intermediates in cells.

To characterize ribosome assembly intermediates, genetic (7–11) and biochemical perturbations (12) in combination with newly developed structural biology tools, have been employed, providing insights into the features of the intermediates and putative assembly pathways. A series of intermediates resulting from the bL17-depletion strain were previously described (13), which revealed five cooperative assembly blocks, and evidence for re-routed assembly pathways under the perturbation of ribosomal protein depletion. Thus far, the studies of the large subunit (LSU) have mostly focused on the late assembly stage (7–11,14–16), while the knowledge about the early assembly of LSU remains limited.

The classical *in vitro* reconstitution of 50S subunits was first achieved by Nierhaus and Dohme (17). Recently, a set of five structures assembled using this protocol provided insights into the final maturation of the peptidyl transferase center (18). While this remarkable *in vitro* reconstitution has provided many intriguing insights into 50S assembly (18–20), the reconstitution reaction is carried out with fully processed and modified rRNAs under non-physiological buffer and temperature conditions, without the participation of assembly factors.

In 2013, Jewett *et al.* reported an *in vitro* integrated rRNA synthesis, ribosome assembly, and translation (iSAT)

*To whom correspondence should be addressed. Tel: +1 858 784 874; Email: jrwill@scripps.edu
†The authors wish it to be known that, in their opinion, the first two authors should be regarded as Joint First Authors.

reaction, which provided a defined system for ribosome biogenesis in a near-physiological environment (21–24). The reagents added into an iSAT reaction include the plasmid encoding the rRNA operon and a reporter gene, a complete set of purified ribosomal proteins, and the cell extract that contains factors and chaperones needed for ribosome biogenesis. By monitoring the translation of a reporter protein, such as GFP or luciferase, the iSAT reaction progress can be observed in real time. In contrast to the classical *in vitro* reconstitution protocol, iSAT is carried out at near-physiological environment (37°C, 10 mM Mg^{2+}) and allows the cascade of transcription, ribosome assembly, and translation to be monitored directly. Importantly, the ribosomes assembled in iSAT can directly perform translation without steps of heat or osmotic activation in the conventional reconstitution method (25).

The iSAT reaction provides a powerful time-resolved platform for structural studies of ribosome assembly intermediates under near-physiological conditions, without being obscured by the vast majority of mature ribosomes *in vivo*. In this work, we succeeded in harnessing the iSAT reaction to capture the very early intermediates during assembly of the ribosomal large subunit and solved their structures by cryo-EM. The set of intermediates can be arranged into a putative temporal order, spanning the assembly landscape from the earliest folding of the 5'-terminal domain I of 23S rRNA (26) to later stages of nearly complete subunits. The landscape exhibits both parallel and sequential folding of cooperative domains, providing a robust process to ensure efficient assembly.

MATERIALS AND METHODS

Purification of native ribosomes and S150 extract

Native ribosomes and S150 extract were purified from S30 crude cell extract as described (22). Briefly, *Escherichia coli* MRE cells were lysed and S30 crude extract was obtained by two clarification spins. The S30 crude extract was layered onto a 10–40% sucrose cushion and ultracentrifugation at 90 000 g and 4°C for 20 h, resulting in a ribosome containing pellet and S150 containing supernatant. Ribosomes were resolved in buffer C (10 mM TrisOAc (pH 7.5 at 4°C), 60 mM NH_4Cl, 7.5 mM $Mg(OAc)_2$, 0.5 mM EDTA, 2 mM DTT) and stored at –80°C. The concentration of 70S ribosomes was determined by A260 readings (1 A_{260} unit = 24 pmol 70S) (27).

The supernatant was centrifuged at 150 000 g and 4°C for 3 h and the top two-thirds of the supernatant was recovered. Using Snake Skin Dialysis tubing (3500 Da MWCO, Thermo fisher) The S150 extract was dialyzed into the AEB storage buffer (10 mM TrisOAc, pH 7.5 at 4°C, 20 mM NH_4OAc, 30 mM KOAc, 200 mM KGlu, 10 mM $Mg(OAc)_2$, 1 mM spermidine, 1 mM putrescine, 1 mM DTT) and concentrated using a 3 kDa MWCO Centriprep concentrators (Merck Millipore). For best performance in the iSAT reaction, the A_{260} and A_{280} of the S150 extract was targeted to be 25 OD and 15 OD, respectively. The protein concentration in the S150 extract was determined by Bradford assay (Thermo Fischer scientific). The S150 extract was stored in small aliquots at –80°C.

Purification of ribosomal proteins

Ribosomal proteins were purified using existing protocols (22,27) with slight modifications: 70S ribosomes were mixed with an equal volume of buffer M (25 mM Tris–HCl pH 7.5, 20 mM $MgCl_2$, 100 mM KCl, 2 mM DTT) containing 8 M Urea and 6 M LiCl, and incubated on ice overnight. After centrifugation at 16 000 g for 15 min at 4°C, the supernatant, containing ribosomal proteins, was collected. The pellet was washed with buffer M containing 8 M Urea and 6 M LiCl, incubated on ice for at least 1 h, and after centrifugation at 16 000 g for 15 min at 4°C, the supernatant was collected. The combined supernatants were dialyzed twice against 100 volumes of buffer M containing 1 M KCl (for 6 h and overnight) using a 1000 Da MWCO Tube-O-Dialyzers (G-Biosciences). The concentration of TP 70 was determined by measuring A_{230} (1 A_{230} unit = 240 pmol TP70). Aliquots were flash frozen and stored at –80°C.

iSAT reaction

The iSAT reaction was performed as described previously (21,22) with slight modifications. Briefly, the iSAT reaction was performed in 57 mM HEPES–KOH, 1.5 mM spermidine, 1 mM putrescine, 10 mM $Mg(Glu)_2$, and 150 mM KGlu at pH 7.5 with 2 mM DTT, 0.33 mM NAD, 0.27 mM CoA, 4 mM oxalic acid, 2% w/v PEG-6000, 2 mM amino acids (Roche), 1 nM pY71sfGFP plasmid encoding superfolder GFP (M. Jewett), 0.1 mg/ml T7 RNA polymerase, 42 mM phosphoenolpyruvate (Roche) and NTP + mix (1.6 mM ATP (Sigma), 1.15 mM of GTP, CTP and UTP each (Sigma), 45.3 μg/μl tRNA from E. coli MRE 600 (Roche), 227.5 μg/μl Folinic acid pH 7.2). The above components were premixed. The final concentration with respect to the total volume of the iSAT reaction is provided. A 5.6 μl aliquot of the premix was pipetted into 6 μl of S150 extract. Ribosomal proteins and plasmid encoding the rrnB operon (pT7rrnb; provided by M. Jewett) were added to a final concentration of 0.4 and 4 nM, respectively. iSAT reactions of 15 μl each were performed in 96-well plates (Applied Biosystems) and incubated in a StepOnePlus Real-time PCR System (Applied Biosystems) at 37°C for variable time. sfGFP production was detected by fluorescence measurement at 5 min intervals (excitation: 450–490 nm, emission: 510–530 nm).

Electron microscopy sample preparation

iSAT reactions were diluted approximately three-fold with buffer E (50 mM Tris pH 7.8, 10 mM $MgCl_2$, 100 mM NH_4Cl, 6 mM β-mercaptoethanol) and loaded onto a 10–40% (w/v) sucrose gradient in buffer E. Gradients were spun in a Beckman SW41 rotor at 26 000 rpm for 12 h and 4°C. Gradient fractions containing ribosomal particles as indicated by A_{260} readings and Agarose gel were spin-concentrated using a 30 kDa MW cutoff filter (Amicon) and the buffer was exchanged to buffer A (20 mM Tris–HCl, 100 mM NH_4Cl, 10 mM $MgCl_2$, 0.5 mM EDTA, 6 mM β-mercaptoethanol; pH 7.5). 3 ul sample was applied to a plasma cleaned (Gatan, Solarus) 1.2 mm hole, 1.3 mm spacing holey gold grid and manually plunge frozen in liquid ethane (28).

Electron microscopy data collection

Single-particle data were collected using Leginon software (29) on a Titan Krios electron microscope (FEI) operating at 300 keV equipped with a K2 Summit direct detector (Gatan) with a pixel size of 1.31 Å at 22 500 magnification. A dose of rate of ∼5.8 e^-/pix/s was collected across 60 frames with a dose of ∼50 $e^-/Å^2$. To overcome problems of preferred orientation, the data was collected at the tilt of –20° (30). A total of 4607 micrographs (15 min: 1655; 35 min: 837; 71 min: 828; 130 min: 565; 240 min: 722) were collected.

Electron microscopy data processing

The micrograph frames were aligned using MotionCor2 (31) within the Appion image processing wrapper (32). All of the subsequent data processing was performed in cryoSPARC (33), as described in Supplementary Figure S2. The micrographs from five iSAT time course datasets were imported into cryoSPARC separately. The CTF parameters were estimated using CTFFIND4 (34). A total of 1 120 554 particles were automatically picked by blobpicker and extracted from the five datasets with default parameters. Two rounds of 2D classification were performed, where 30S and 70S particles are removed from the dataset. 900 883 particles were selected and used for the iterative subclassifications.

For ribosome assembly intermediate datasets, the goal of data processing is to reconstruct a diverse set of as many intermediate classes as possible at an interpretable resolution. An iterative subclassification approach (35) was used where *ab initio* reconstructions were performed to reach the above goal. The first round of *ab initio* reconstruction was performed specifying 5 classes, resulting in elimination of 726 204 'junk' particles in the first round of classification. We attempted to rescue additional classes from these junk particles with another two rounds of *ab initio* reconstructions, but no meaningful classes emerged, and these particles were discarded. The classes displaying clear RNA structural features were selected for the subsequent subclassification and reconstruction. The remaining classes were subjected to another round of *ab initio* reconstruction to confirm that the respective particles could be excluded from further analysis. The selected classes were then subclassified by iterative *ab initio* reconstructions. The number of subclasses specified at any given stage depend on the number of the particles in the class (more than 100 000: five classes, 10 000–100 000: four classes, <10 000: three classes). When the number of particles in a reconstructed class is <2000, subclassification was terminated and the particles of the class were subjected to homogeneous refinement. All parameter settings for refinement were default in cryoSPARC. Classes that failed to provide a high-resolution reconstruction (worse than 10 Å) were discarded. After the iterative subclassification, a total of 102 863 particles were classified and reconstructed into 30 density maps.

During the iterative subclassification, the major classes are independently divided into smaller classes, and particles that are mis-assigned early in subclassification can be separated out and reconstructed during the later subclassifications. Therefore, it is possible that similar maps can emerge from different initial major classes, and these similar maps should be identified and combined. To determine the differences between the set of 30 maps, the pairwise molecular weight difference was calculated among all the thirty maps, and these differences were used as the metric for hierarchical cluster analysis, as described before (35). A 10.0 kDa threshold was chosen for identifying maps that were essentially similar, and the particles from such classes were combined, repeating the *ab initio* reconstruction (with 1 class) and homogenous refinement. After clustering and combining, thirteen distinct density maps were reconstructed with global resolutions ranging from 4.5 to 8.8 Å. Figures of the density maps in this manuscript were prepared using UCSF Chimera X (36).

Quantitation of rRNA and protein occupancy in EM density maps

The crystal structure of *E. coli* 50S subunit (PDB: 4YBB) was segmented into 139 elements and binarized to serve as a reference surface (13,35). The density maps of iSAT time course intermediates were binarized with the threshold voxel level = 1. The relative values between the density maps and the reference surface maps were calculated, resulting in the occupancy values between 0 and 1 for each element. The occupancy value for each element was binarized with thresholds determined in Supplementary Figure S12. The occupancy values were hierarchically clustered using Euclidean distance with Ward linkage. The clustered elements were combined and defined as cooperative assembly blocks.

Dependency analysis for the cooperative assembly blocks

The quadrant analysis was used to analyze the dependency between the cooperative assembly blocks. A scatterplot was generated of the occupancy values for element i and element j of all density maps. As the occupancy values were binarized according to the procedure above, the points on the scatter plot (*i*,*j*) will have four possible coordinate values: (0,0), (0,1), (1,0), (1,1). The dots of the elements that were defined into a cooperative assembly block could be treated as one point. For each scatter plot, if the coordinates of the points are only (0,0), (0,1), (1,1) or (0,1), (1,1), meaning the block *i* always presents with the presence of block *j*, then block i is considered to have dependency to block *j*. If the coordinates of the dots are only (0,0), (1,0), (1,1) or (1,0), (1,1), block *j* is considered to be dependent on block *i*.

In the dependency map shown in Figure 4, the arrows indicate the dependencies between the blocks. For a parsimonious and clear view of the dependency map, only the closest dependencies were plotted. For example, if block c has dependencies a → c and b → c, and block b has dependency a → b, the a → c dependency is pruned, giving the concise dependencies a → b → c.

Quantitative mass spectrometry of ribosomal proteins

To quantify the protein composition of iSAT ribosomes, ribosomal proteins were prepared as described (13). In brief, 50 pmol of ^{14}N labelled iSAT ribosomes were mixed with

an equal amount of ^{15}N labelled WT ribosomes purified from *E. coli* MRE600 cells. Proteins were precipitated in 13% trichloroacetic acid (TCA) overnight at 4°C, pelleted by centrifugation at 14 000 rpm for 30 min at 4°C. The pellet was washed once in 700 μl cold 10% TCA and once in 700 μl cold acetone. The air-dried pellet was re-dissolved in 40 μl 100 mM NH_4HCO_3, 5% acetonitrile (ACN), 5 mM DTT and incubated at 65°C for 10 min. Subsequently, 10 mM iodoacetamide (IAA) was added and the sample was incubated at 30°C for 30 min in the dark. The proteins were digested by 0.2 μg modified grade porcine trypsin (Promega, Co., Madison, WI) during overnight incubation at 37°C. The next day, peptides were purified using Pierce C18 Spin column (Thermo scientific) following the manufacturers protocol. Peptides were eluted from the column by adding 60 μl of 70% ACN, 0.1% formic acid and the eluent was dried in a Speed-Vac concentrator. Prior to MS analysis, the samples were re-dissolved in 10 μl MS Buffer (5% ACN, 0.1% formic acid) and centrifuged for 10 min at high speed. 4 μl sample were mixed with 1 pmol of a retention time calibration mixture (IRT, Pierce).

SWATH-MS was acquired on a Sciex 5600+ TripleTOF mass spectrometer coupled to an Eksigent nano-LC 400 system. Using the auto sampler, peptides were injected onto a SB-C18 Nano HPLC column (0.5 × 150 mm, Agilent Zorbax), and resolved using a 120 min gradient from 5 to 45% acetonitrile in 0.1% formic acid. SWATH data-independent acquisition was obtained in positive ion mode over the 400–1200 m/z range. The mass spectral data analysis and r-protein quantification against the ^{15}N-labeled reference was performed using Skyline (37).

Quantitative mass spectrometry of rRNA modifications

Quantitative analysis of rRNA modifications in iSAT ribosomes has been carried out relative to modifications present in 70S rRNA isolated and purified from ^{15}N-labeled *E. coli* MRE600 cells. rRNA isotope labeling, isolation and purification using sucrose gradient ultracentrifugation has been carried out as described in prior work (38). Replicate analysis has been performed using two independent iSAT preparations, from which sucrose fractions corresponding to iSAT 70S ribosomes have been combined and used for LC–MS sample preparation. For Replicate 1, isolated and purified iSAT rRNA were combined with wild-type ^{15}N-labeled rRNA in about equal molar ratio based on A_{260}, digested using RNase T1 or A for 1 h at 55°C in 25 mM ammonium acetate (pH =6), then subjected to LC–MS analysis. For Replicate 2, iSAT rRNA were first combined with wild-type ^{15}N-labeled rRNA and then derivatized with CMCT (*N*-cyclohexyl-*N*′-(2-morpholinoethyl)carbodiimide metho-p-toluenesulfonate, Sigma-Aldrich) reagent based on protocol published by Carlile *et al.* (39). Specifically, rRNA pellet has been dissolved in 20 μl volume of 0.4 M CMCT in BEU buffer (50 mM Bicine (pH 8.5), 4 mM EDTA (pH 8.0), 7 M urea), and incubated at 37°C for 1h. Then, rRNA has been purified from excess of CMCT using 0.5 ml 30 kDa Amicon Ultra filter with two rounds of exchange to RNase-free water. The recovered 30–40 μl of rRNA were combined with an equal volume of 100 mM sodium carbonate-bicarbonate buffer (pH 10.5) and incubated at 50°C for 2 h. Following additional two rounds of 30 kDa Amicon buffer exchange to RNase-free water, CMC-derivatized rRNA has been freeze-dried and subjected to the RNase digestion. CMCT protocol used resulted in 60–90% efficient labeling of all rRNA pseudouridines, without significant number of off-target identifications. A single CMC chemical tag adds 251.2 Da to the mass of underivatized nucleolytic RNA, and furthermore increases its retention of the reverse-phase column, thus permitting specific detection of pseudouridines in addition to rRNA methylation.

LC–MS data were acquired on Agilent Q-TOF 6520 ESI instrument coupled to the Agilent 1200 LC system. rRNA digestion fragments were chromatographically resolved on XBridge C18 column (3.5 μM, 1 × 150 mm, Waters) using 15 mM ammonium acetate (pH 8.8) as mobile phase A and 15 mM ammonium acetate (pH = 8.8) in 50% acetonitrile as mobile phase B. 50 min long linear gradient was constructed: 1–15% of B over 40 min (corresponds to elution of underivatized RNA), followed by 15–35% of B over 10 min (corresponds to elution of CMC-derivatized RNA). Negative ionization data were recorded over the 400–1700 m/z range. Pairs of the co-eluting ^{14}N- and ^{15}N-labeled fragments were identified using their predicted m/z values. MS peak profiles were extracted, averaged over a 0.1 min wide window, and quantitatively fit to their theoretical isotope distribution using Isodist (40). The ratios of ^{14}N- and ^{15}N-peak amplitudes were used to calculate modification fractions for individual rRNA modifications, after they were normalized to the ratios for unmodified 16S or 23S rRNA transcripts (38).

RESULTS AND DISCUSSION

Assembly of the ribosome in iSAT is near-native

In the iSAT reaction, the primary rRNA transcript is transcribed in the presence of processing enzymes, r-proteins, and assembly factors, allowing for co-transcriptional ribosome assembly under near-physiological conditions (41). The production of active ribosomes is monitored by their translation of a fluorescent reporter protein (sfGFP) (Figure 1A). The fluorescence signal starts to rise after a lag of about 20 min. When purified 70S ribosomes were added to the reaction instead of the plasmid encoding rRNA and purified total ribosomal proteins, the fluorescence signal rises without a lag (Figure 1B), indicating that the signal lag observed in the iSAT reaction can be attributed to the transcription of rRNA and the assembly of the ribosome. The fluorescence signal reaches a plateau after 2 h (Figure 1B), which is likely due to exhaustion of the ATP supply (41). In comparison with the ribosome profile for the 70S ribosome control, the sucrose gradient profile of a 4-hour iSAT reaction (Figure 1C) indicates the presence of a pre-50S peak in addition to the 30S peak and a much smaller 70S peak. The pre-50S peak can be characterized to provide information about the ribosome assembly process.

In the iSAT reaction, rRNA and mRNA are transcribed by T7 RNAP, instead of the native *E. coli* RNAP, which interacts with Nus factors in rRNA transcription elongation complexes and modulates ribosome biogenesis in *E. coli* cells (42,43). Fritz *et al.* have extensively optimized the iSAT system for activity by tuning of the concentration of

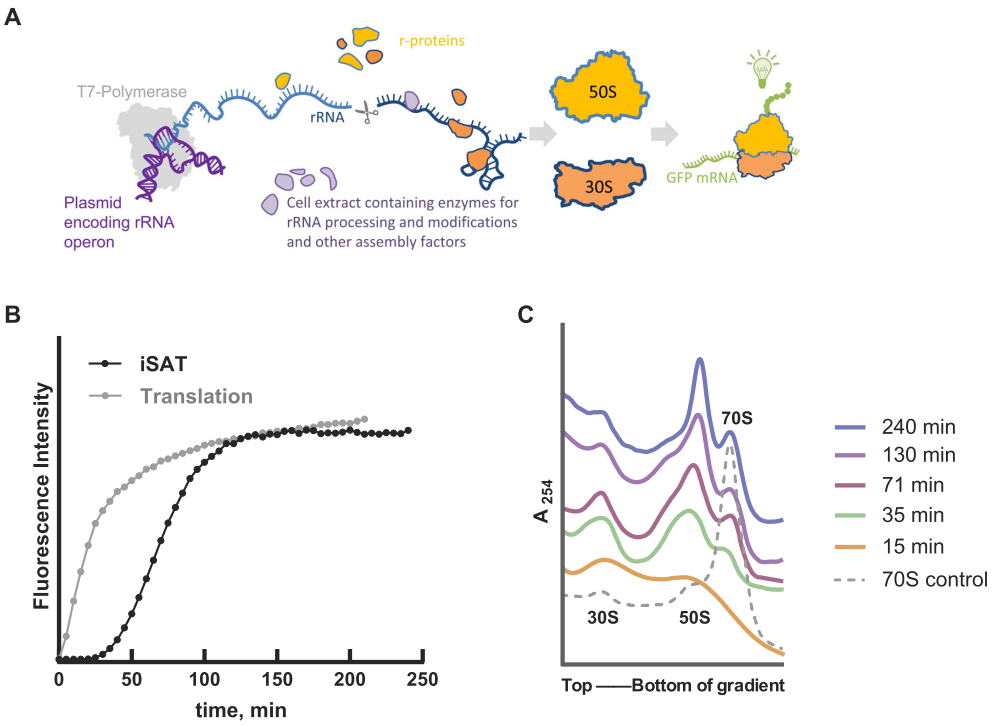

Figure 1. Time course of the integrated rRNA synthesis, ribosome assembly, and translation (iSAT) reaction. (**A**) Schematic of the iSAT reaction. In an iSAT reaction, plasmids encoding rRNA and a reporter mRNA are transcribed by T7 polymerase. The rRNA is processed and modified by enzymes in an *E.* coli cell extract, and ribosomal proteins derived from purified ribosomes bind to complete the ribosomal subunits. Newly assembled ribosomes engage in the translation of the reporter protein (GFP) producing a readout that visualizes the production of functional ribosomes. (**B**) Fluorescence readout of iSAT. The time course of GFP fluorescence is shown for a standard iSAT reaction (black), compared to a control reaction where intact ribosomes were directly added into the reaction (gray). The delay of fluorescence signal in the iSAT reaction is due to assembly of sufficient ribosomes to produce GFP. (**C**) Ribosome profile of iSAT time course reactions. Five parallel iSAT reactions were quenched at sequential time points, and the ribosome profiles of the iSAT reactions were analyzed using sucrose density gradient ultracentrifugation. In general, both the size and abundance of ribosome precursors increases over time.

rRNA encoding plasmids and T7 RNAP (22). Although Lewicki et al. reported that substitution of T7 RNAP for endogenous RNAP cannot produce active ribosomes in *E. coli* cells (44), T7 RNAP is efficient *in vitro*, probably because the rRNA transcription rate can somehow match the ribosome assembly rate in the iSAT system (22). To characterize if the ribosomes assembled in the iSAT reaction resemble the ribosomes in cell, the 70S ribosomes produced during iSAT were analyzed for their protein composition and rRNA modifications using quantitative mass spectrometry (Supplementary Figure S1). Most ribosomal proteins were present in stoichiometric amounts compared to purified 70S ribosomes from MRE600 cells, except that bL33 was reduced by 53%. Post-transcriptional modifications of ribosomal RNA play a critical role in the assembly process, with consequences for RNA folding, ribosome activity and susceptibility to metabolites (45–47). Remarkably, we found that most nucleotide modification sites on both 16S and 23S rRNAs were properly installed in the iSAT reaction (Table S1), which supports the idea that the recruitment of rRNA modification enzymes from the cell extract during the iSAT reaction resembles the native process *in vivo*. In summary, the ribosomes assembled in iSAT system are near-native, and iSAT provides an opportunity to study the ribosome assembly process in a near-physiological environment.

Time-resolved *in vitro* assembly of the LSU

The iSAT reaction is both continuous and asynchronous, and it is likely that there is a pool of assembling 50S intermediates over the time-course of the reaction, with accumulation of completed 50S over time. To capture and examine an array of the 50S intermediates of various stages, the iSAT reaction was quenched on ice at a series of timepoints. We chose a 15-min timepoint from the lag phase, 35- and 71-min timepoints from the phase with linear GFP synthesis, a 130-min timepoint corresponding to the very beginning of the plateau phase, and a 240-min timepoint from the exhaustion phase. (Figure 1B). The sucrose gradient profiles of the reaction mixture showed that the particle size generally increased with time (Figure 1C), implying the presence of more immature pre-50S particles at earlier timepoints, and the opportunity to examine a range of intermediate structures.

Cryo-EM single-particle analysis and iterative *ab initio* subclassification reveals new LSU assembly intermediates

To gain structural insights into the dynamic assembly process over the course of the iSAT reaction, we employed single-particle cryo-EM. For each timepoint, we applied all rRNA containing fractions from the sucrose gradient onto holey gold grids and collected datasets on the Titan Krios

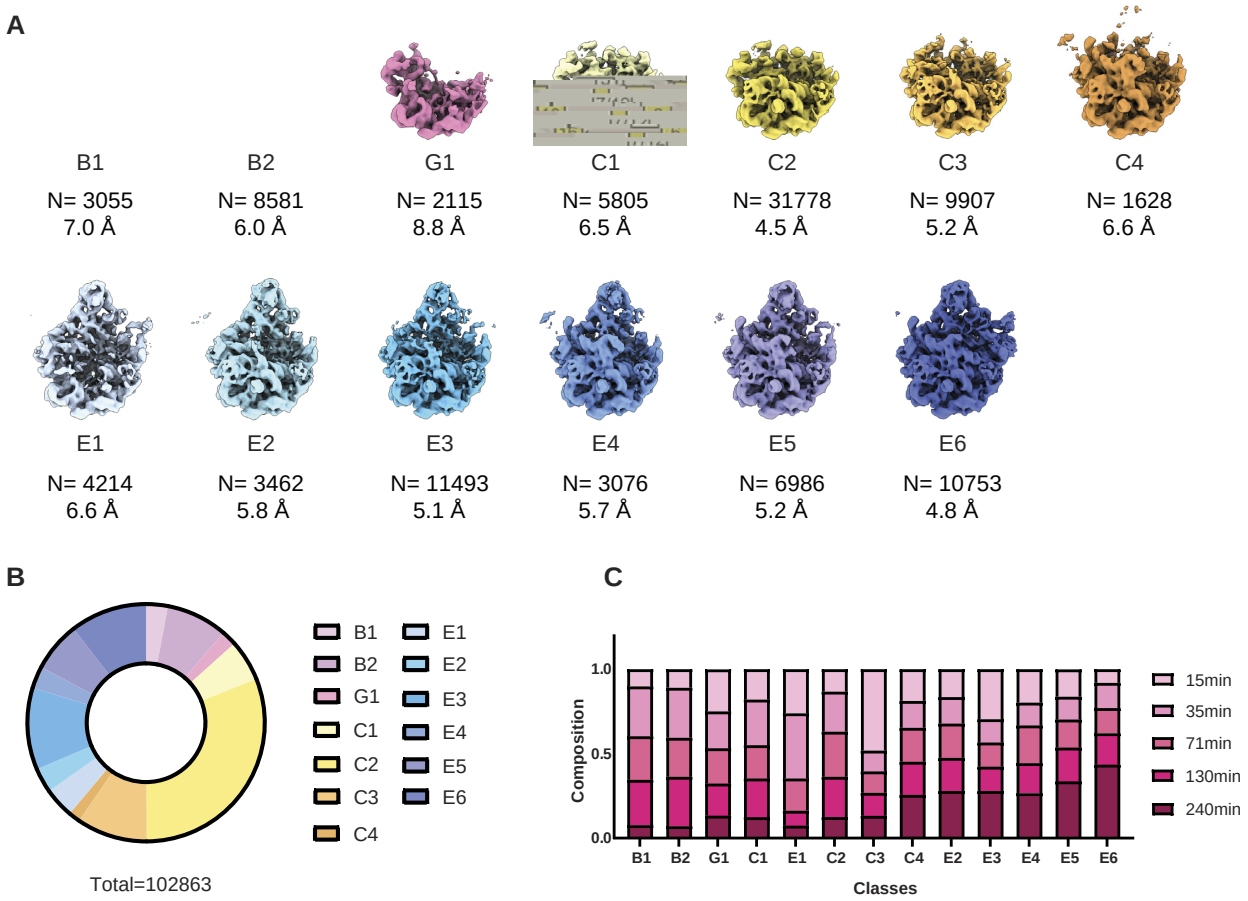

Figure 2. Distribution of 50S intermediates in the iSAT reaction time course. (**A**) Density maps for 50S intermediates. Thirteen 50S intermediates were obtained by heterogeneous subclassification from the iSAT reaction time course, where all timepoints were combined prior to analysis. The thirteen 50S precursors are named according to the major class they belong to, and are generally ordered from immature to mature. The number of particles contributing to each class is given along with the final resolution of the map. (**B**) Particle class distribution among the 50S intermediates. The particle distribution among 50S precursors was calculated according to the number of particles reconstructing each class (Table S2). (**C**) Temporal composition of 50S intermediates. The contribution of each timepoint to each 50S intermediates class was calculated and plotted in the bar plot. First, the number of the particles was normalized in each dataset of the five timepoints. Subsequently, the particle contribution of each timepoint to each class was calculated. In general, less mature classes have a higher contribution from the earlier timepoints, and the more mature classes have a higher contribution from the later timepoints. The production of ribosomes is continuous during the iSAT reaction, and it is expected that all classes could be observed at any time point.

transmission electron microscope equipped with a K2 direct electron detector. These efforts yielded five separate datasets for downstream analyses using computational classification.

Samples containing assembly intermediates from the iSAT reaction are inherently heterogeneous and are additionally marred by contaminants from non-50S particles and/or the cellular milieu. To analyze the highly heterogenous cryo-EM datasets from our iSAT reaction, we developed an iterative subclassification workflow using cryoSPARC (33) (Supplementary Figure S2). Blob-picker was employed for particle selection to prevent any bias from using a template, with the goal of picking all possible particles that might represent intermediates. To reconstruct as many classes as possible, especially the minor classes, the particles extracted from motion-corrected micrographs of all five time-course datasets were pooled together for processing. Two rounds of 2D classification were performed to remove the particles that visually did not resemble pre-50S intermediates, such as 30S and 70S particles. Subsequently, the remaining particles were iteratively subclassified using *ab initio* reconstruction, until there were not enough particles in a given subclass to provide a 10 Å reconstruction. Due to our loose criteria for particle selection, about 80% of the particles failed to be included in classes in the first round of *ab initio* reconstruction, and were accordingly discarded. Most of the junk particles could be easily eliminated during the initial classification step, so that the eventually reconstructed classes can cover most of the 50S intermediates existing in the iSAT reaction. No additional classes could be rescued from subclassification of the discarded particles.

The final maps resulting from the iterative subclassification were refined by homogeneous refinement. The density maps were compared by hierarchical analysis and combined as previously described (35). Thirteen distinct maps were identified from all time-course datasets, as shown in Figure 2A. The resolutions of the maps vary from 4.5 Å to 8.8 Å (Supplementary Figure S3), where the resolutions

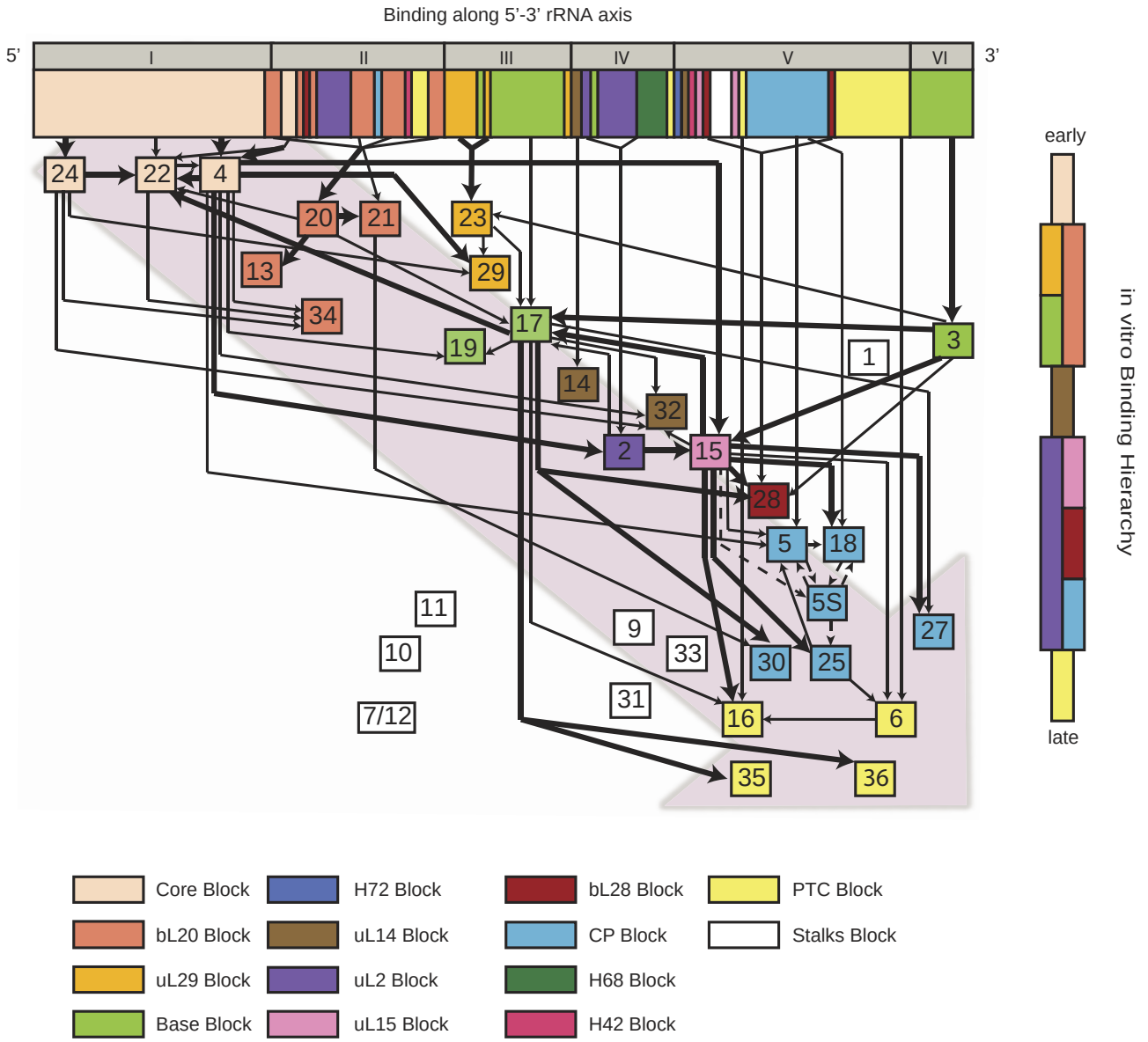

Figure 5. Updated Nierhaus assembly map including assembly block hierarchy. The original protein dependencies from the Nierhaus assembly map are shown as thick and thin black arrows, for strong and weak dependencies. The 23S rRNA bar is annotated both with the domain designation and colored according to the iSAT assembly blocks. The order of the block dependencies in Figure 4 is shown on the right to indicate early to late progress. The positions of the ribosomal proteins are rearranged horizontally according to the position of the interacting rRNA helices in the same block, and rearranged vertically according to the dependencies of the assembly. The newly observed block dependencies are consistent with the original Nierhaus assembly map and with a 5' to 3' co-transcriptional direction of assembly.

bly blocks. The vertical axis was arranged according to the block dependencies, with early blocks on the top and later blocks on the bottom. After the rearrangement, most of the r-proteins naturally fall on a general trend line (shown in pink arrow in Figure 5), from the top left to bottom right. The general trend line clearly demonstrated the 5'-3' progression of the cooperative assembly blocks during LSU assembly (20,50,51). Also, most of the arrows retained from the Nierhaus map had the direction from top to bottom, which was consistent with the block dependency. In brief, the updated Nierhaus assembly map illustrates more detailed information about the interactions between the r-proteins and the rRNA helices, which also provides evidence for the co-transcriptional direction for assembly.

Early LSU biogenesis reveals a common precursor and a strong co-transcriptional directionality

The Core Block, as shown in Figure 6A, is the intersection of density for the B1 and G1 classes. It is the smallest common precursor of LSU assembly that has been reported so far. The structure of a similar assembly core was identified in another dataset from a Δ*deaD* deletion strain (submitted), which confirmed the shared pathway under *in vivo* and *in vitro* conditions and also the important role of this as-

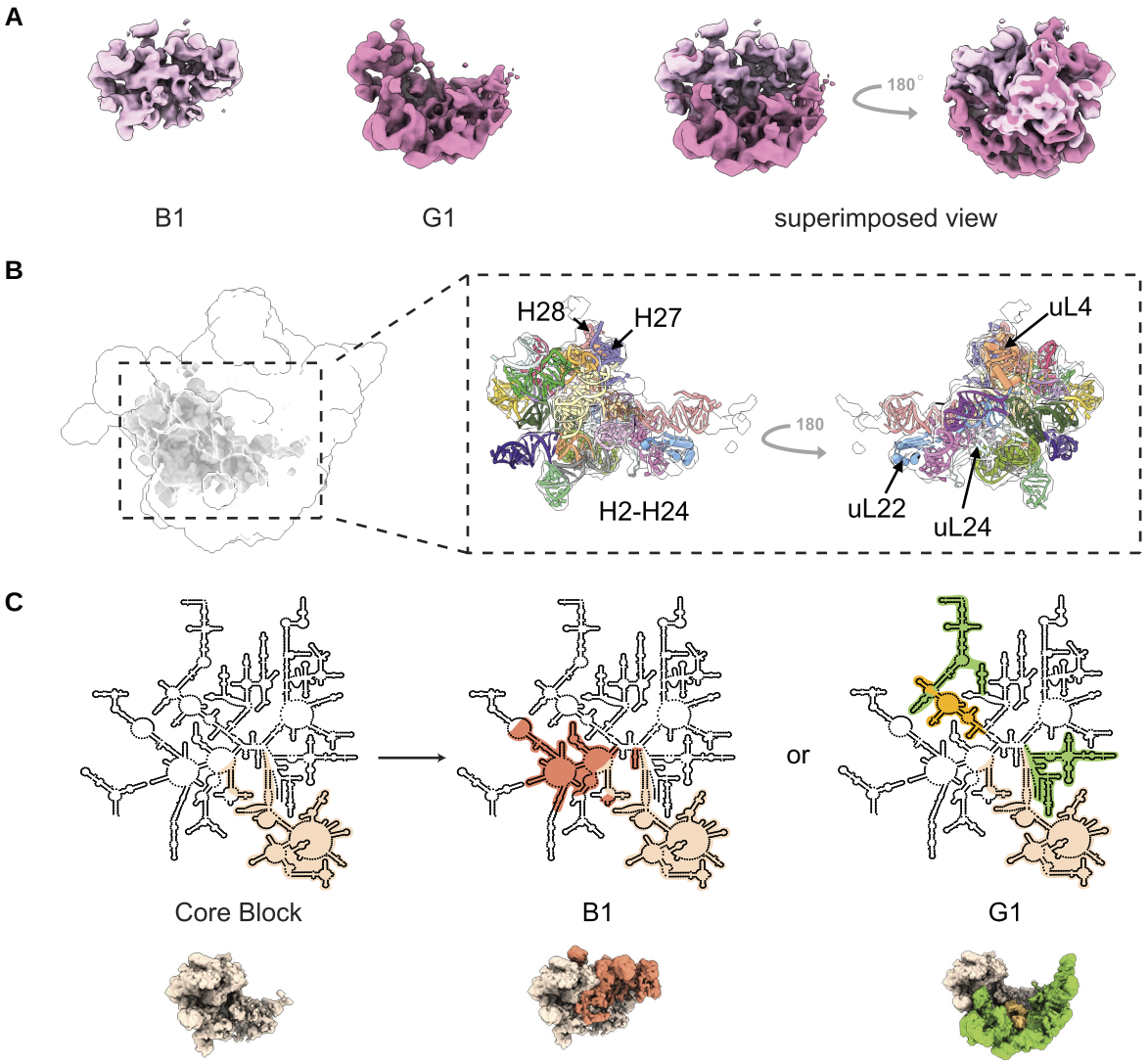

Figure 6. Evidence for parallel steps early in assembly. (**A**) The superimposed structures of 50S intermediates B1 (light pink) and G1 (dark pink). The density region in common between the B1 and G1 classes corresponds to the Core Block. (**B**) The Core Block comprises primarily domain I. The position and structure of the assembly Core Block are displayed. The rRNA helices and ribosomal proteins uL4, uL22 and uL24 are labeled, consistent with formation of domain I as the earliest step in assembly (Figure 5). (**C**) Parallel pathway early in assembly. Formation of the B1 class and the G1 class occurs by consolidation of either domain II (for B1) or domains III/VI (for G1) to the Core Block, indicating two parallel pathways after the folding of the Core Block. The rRNA secondary structure maps are colored according to the blocks. The theoretical densities of the corresponding blocks are generated from the 50S crystal structure (PDB: 4YBB) and displayed below the secondary structure maps. The color codes are consistent with the previous figures.

sembly core at early stages of biogenesis. The Core Block is composed of the majority of 23S rRNA domain I (H2–24), a small part of domain II (H27-28), and three ribosomal proteins: uL4, uL22 and uL24, which primarily bind to domain I rRNA (20,52–54) (Figure 6B). All these helices are located at the very 5'-end of the 23S rRNA, which supports co-transcriptional ribosome assembly (19,55,56).

The analysis of block composition for each class suggests parallel and modular assembly pathways (Figure 7 and Supplementary Figure S11). After the formation of a common precursor, the Core Block, there are two parallel pathways to get to C1, one through a B class and another through an intermediate G class (Figure 6C and Figure 7). Proceeding from the Core Block to C1 class through B classes, the assembly follows the directionality of 5'-to-3' transcription (Figure 6C), sequentially adding the central part of domain II and domain III and corresponding r-proteins to the core. Interestingly, those absent helices in domain II and III, such as H42-44 and H55-58, correlate well with later emergence in the evolution process (57). After the B class, the closing of the 5' and 3'-end of the 23S occurs in the transition of B2 to C1 through the Base Block. On the other hand, the pathway through the G1 class, shows the docking of the Base Block and the uL29 Block before the bL20 Block (Figure 6C and Figure 7), which is an apparent alternative pathway with a small population in the ensemble (Figure 2B).

As mentioned above, the generation of a new ribosome takes about two minutes *in vivo* (5). However, the transcription of an rRNA precursor was estimated to be completed in over one minute at a rate of 70–80 nt/s (58,59).

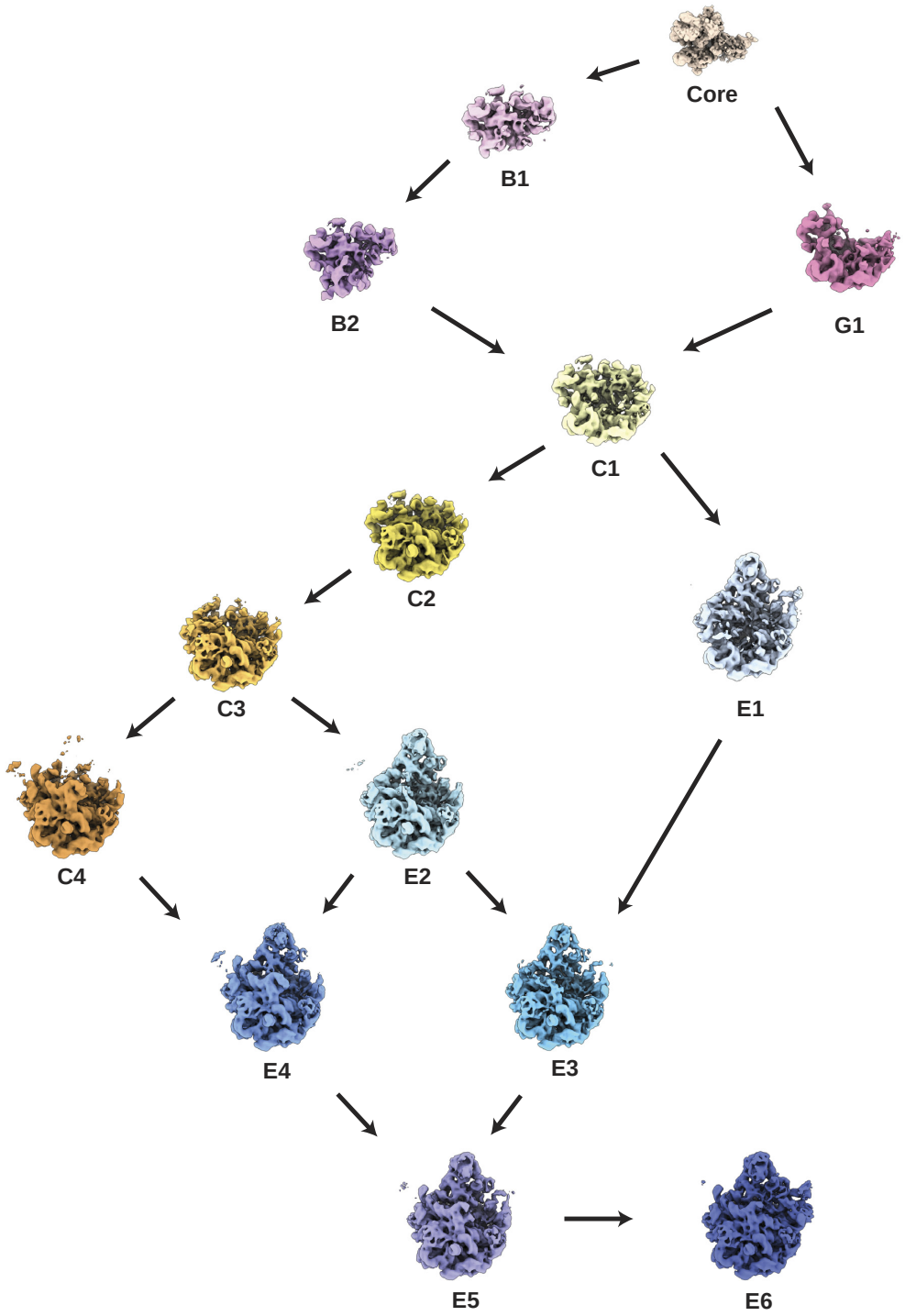

Figure 7. Organization of 50S intermediates into an assembly pathway. The thirteen reconstructed 50S intermediates from the iSAT reaction are organized according to the dependencies of the assembly blocks. The arrows indicate the minimal folding steps required to connect the set of intermediates. The theoretical density of the Core Block is shown according to the 50S PDB model 4YBB.

Therefore, although the assembly of ribosome is likely to be co-transcriptional, the transcription of rRNA is still faster than the docking of folded domains, which is also supported by the close of 5'- and 3'-ends resolved in the Base Block from our dataset. It is likely that at this early assembly stage, other domains that have been transcribed can fold independently but are dangling in various states of organization. The docked Base block also implies strong interdomain interactions between domain III and domain VI, which is likely realized by the 'retrograde' interaction of protein L3 (Figure 5). The 5' to 3' gradient we observe is the consolidation of interdomain interactions roughly in the order of domain I, II, III. To ensure the translation fidelity, it is reasonable that domain VI docks earlier than domain V, which includes the peptidyl transferase center (PTC) active site that forms in the final steps.

Complexity of late LSU biogenesis resulted from block independency

Unlike early blocks, the late blocks become more independent, leading to a complicated and parallel assembly trajectory (Figure 7 and Supplementary Figure S11). From the C1 to the C4 class, increasing density of H38 was observed (Supplementary Figure S8B), indicating the maturation of this long bridge helix. The most significant feature of the C2 class is the formation of blocks at the 'belly' of the subunit: uL14 Block and uL2 Block. After that, the C3 class forms the uL15 Block, which is another key block required for docking of the CP Block. According to the Nierhaus map and Figure 5, uL15 has multiple interactions with the r-proteins in the CP Block (20), and it is a critical protein for the initiation of the assembly of the CP (60). With the uL15 Block assembled, the C3 class is ready for the assembly of the bL28 Block, and subsequently the docking of the CP Block.

From the C3 class, either the H68 Block or the CP Block is ready to assemble. In the C3-C4–E4 pathway, the H68 Block first assembles to form the C4 class, then the CP Block assembles to form the E4 class, while the C3–E2–E4 pathway is an alternative order of these transitions. The increased density of the H42 Block in the E3 class is the primary distinction from the E4 class. Compared with the left pathways in Figure 7, in which uL2 Block assembled first, the transition of E1 to E5 on the right opened an alternative mechanism of assembling CP, uL14, uL15 and bL28 Blocks first, followed by uL2 Block. The presence of E1 indicates the high parallel and modular feature of 50S assembly at late stage. In the last step, with all the above blocks assembled, the E5 class can support formation of the PTC block to reach the E6 class, which is the most mature class resolved in the iSAT intermediate library.

Consistent with recent *in vitro* and *in vivo* studies, the functional core of ribosome subunit always assembles at the latest stages (8–11,13–15,18). Intriguingly, the C4 class can exhibit partially mature P and E sites for tRNA binding prior to the docking of the central protuberance, while some early E classes also have mature P and E sites with a docked central protuberance. Therefore, ribosome assembly in the iSAT system strictly produces the tRNA A site in the last step of the maturation. The intermediates with partially matured P, E and A functional sites, but with no central protuberance were only observed in a suppressor mutation strain resulted by the activity-reduced mutation of RbgA (61), which is a case where the normal timing of the maturation of the functional sites was perturbated by the lack of a vital assembly factor.

In summary, the iSAT reaction provides a wealth of information about the intermediates that accumulate during assembly of the 50S subunit under near-physiological conditions. The intermediates share common features with previous datasets resulting from perturbed growth in cells or *in vitro* reconstitution (7,13,18). In addition, a significant series of novel early intermediates were identified that provide the earliest known intermediates to date for 50S assembly. The features of parallel and sequential assembly steps appear to be ubiquitous on the ribosome assembly landscape, although the assembly is generally consistent with the direction of rRNA synthesis.

The validation of iSAT as a platform for assembly offers many fascinating possibilities to study ribosome biogenesis. First, the flexibility of the iSAT reaction conditions will provide a powerful tool to further probe the mechanistic roles of individual assembly factors that are critical for efficient assembly under a variety of conditions in cells. Further, there is the possibility of studying perturbations that are lethal to cells. Second, since ribosome assembly coexists with rRNA transcription and processing in the iSAT system, *in situ* information could be obtained through cryo-electron tomography (cryo-ET), which provides an opportunity to directly image the ultrastructure of the rRNA transcription complexes together with the assembling ribosomal particles. Overall, the results from the iSAT reaction will provide a powerful complement to studies in cells and *in vitro* reconstitution approaches in tackling the mechanistic understanding of ribosome biogenesis.

DATA AVAILABILITY

Novel software tools and the cryo-EM map files utilized in this manuscript have been deposited at https://github.com/FishDong2333/iSAT_Dong_2022.git. The density maps have been deposited in the EMDB with the following accession numbers: Class B1: EMD-29056, Class B2: EMD-29042, Class G1: EMD-29057, Class C1: EMD-29058, Class C2: EMD-29059, Class C3: EMD-29060, Class C4: EMD-29061, Class E1: EMD-29062, Class E2: EMD-29063, Class E3: EMD-29064, Class E4: EMD-29065, Class E5: EMD-29066, Class E6: EMD-29067. The mass spectrometry proteomics data have been deposited to the ProteomeXchange Consortium via the PRIDE partner repository with the dataset identifier PXD038716.

SUPPLEMENTARY DATA

Supplementary Data are available at NAR Online.

ACKNOWLEDGEMENTS

We thank Michael C. Jewett and Anne E. d'Aquino for the iSAT plasmids and their help with setting up the iSAT reaction.

FUNDING

National Institutes of Health [GM136412, GM053757 to J.R.W., U54 AI170855 to D.L.]; Hearst Foundations Developmental Chair (to D.L.); Human Frontier Science Program [LT000465/2017 to L.K.D.]. Funding for open access charge: Institutional unrestricted funds.
Conflict of interest statement. None declared.

REFERENCES

1. Friesen,J.D. (1988) *Escherichia coli* and *Salmonella typhimurium*: cellular and molecular biology. *Science*, **240**, 1678–1681.
2. Shajani,Z., Sykes,M.T. and Williamson,J.R. (2011) Assembly of bacterial ribosomes. *Annu. Rev. Biochem.*, **80**, 501–526.
3. Pletnev,P., Guseva,E., Zanina,A., Evfratov,S., Dzama,M., Treshin,V., Pogorel'skaya,A., Osterman,I., Golovina,A., Rubtsova,M. *et al.* (2020) Comprehensive functional analysis of *Escherichia coli* ribosomal RNA methyltransferases. *Front. Genet.*, **11**, 97.
4. Wilson,D.N. and Nierhaus,K.H. (2007) The weird and wonderful world of bacterial ribosome regulation. *Crit. Rev. Biochem. Mol. Biol.*, **42**, 187–219.
5. Chen,S.S., Sperling,E., Silverman,J.M., Davis,J.H. and Williamson,J.R. (2012) Measuring the dynamics of E. coli ribosome biogenesis using pulse-labeling and quantitative mass spectrometry. *Mol. Biosyst.*, **8**, 3325–3334.
6. Lindahl,L. (1975) Intermediates and time kinetics of the in vivo assembly of *Escherichia coli* ribosomes. *J. Mol. Biol.*, **92**, 15–37.
7. Rabuck-Gibbons,J.N., Popova,A.M., Greene,E.M., Cervantes,C.F., Lyumkis,D. and Williamson,J.R. (2020) SrmB rescues trapped ribosome assembly intermediates. *J. Mol. Biol.*, **432**, 978–990.
8. Jomaa,A., Jain,N., Davis,J.H., Williamson,J.R., Britton,R.A. and Ortega,J. (2014) Functional domains of the 50S subunit mature late in the assembly process. *Nucleic Acids Res.*, **42**, 3419–3435.
9. Li,N.N., Chen,Y.L., Guo,Q., Zhang,Y.X., Yuan,Y., Ma,C.Y., Deng,H.T., Lei,J.L. and Gao,N. (2013) Cryo-EM structures of the late-stage assembly intermediates of the bacterial 50S ribosomal subunit. *Nucleic Acids Res.*, **41**, 7073–7083.
10. Ni,X., Davis,J.H., Jain,N., Razi,A., Benlekbir,S., McArthur,A.G., Rubinstein,J.L., Britton,R.A., Williamson,J.R. and Ortega,J. (2016) YphC and YsxC GTPases assist the maturation of the central protuberance, GTPase associated region and functional core of the 50S ribosomal subunit. *Nucleic Acids Res.*, **44**, 8442–8455.
11. Seffouh,A., Jain,N., Jahagirdar,D., Basu,K., Razi,A., Ni,X., Guarne,A., Britton,R.A. and Ortega,J. (2019) Structural consequences of the interaction of RbgA with a 50S ribosomal subunit assembly intermediate. *Nucleic Acids Res.*, **47**, 10414–10425.
12. Stokes,J.M., Davis,J.H., Mangat,C.S., Williamson,J.R. and Brown,E.D. (2014) Discovery of a small molecule that inhibits bacterial ribosome biogenesis. *Elife*, **3**, e03574.
13. Davis,J.H., Tan,Y.Z., Carragher,B., Potter,C.S., Lyumkis,D. and Williamson,J.R. (2016) Modular assembly of the bacteria large ribosomal subunit. *Cell*, **167**, 1610–1622.
14. Arai,T., Ishiguro,K., Kimura,S., Sakaguchi,Y., Suzuki,T. and Suzuki,T. (2015) Single methylation of 23S rRNA triggers late steps of 50S ribosomal subunit assembly. *Proc. Natl. Acad. Sci. U.S.A.*, **112**, E4707–E4716.
15. Wang,W., Li,W., Ge,X., Yan,K., Mandava,C.S., Sanyal,S. and Gao,N. (2020) Loss of a single methylation in 23S rRNA delays 50S assembly at multiple late stages and impairs translation initiation and elongation. *Proc. Natl. Acad. Sci. U.S.A.*, **117**, 15609–15619.
16. Nikolay,R., Hilal,T., Schmidt,S., Qin,B., Schwefel,D., Vieira-Vieira,C.H., Mielke,T., Bürger,J., Loerke,J., Amikura,K. *et al.* (2021) Snapshots of native pre-50S ribosomes reveal a biogenesis factor network and evolutionary specialization. *Mol. Cell*, **81**, 1200–1215.
17. Nierhaus,K.H. and Dohme,F. (1974) Total reconstitution of functionally active 50S ribosomal subunits from Escherichia coli. *Proc. Natl. Acad. Sci. U.S.A.*, **71**, 4713–4717.
18. Nikolay,R., Hilal,T., Qin,B., Mielke,T., Burger,J., Loerke,J., Textoris-Taube,K., Nierhaus,K.H. and Spahn,C.M.T. (2018) Structural visualization of the formation and activation of the 50S ribosomal subunit during in vitro reconstitution. *Mol. Cell*, **70**, 881–893.
19. Nierhaus,K.H. (1991) The assembly of prokaryotic ribosomes. *Biochimie*, **73**, 739–755.
20. Herold,M. and Nierhaus,K.H. (1987) Incorporation of six additional proteins to complete the assembly map of the 50 S subunit from Escherichia coli ribosomes. *J. Biol. Chem.*, **262**, 8826–8833.
21. Jewett,M.C., Fritz,B.R., Timmerman,L.E. and Church,G.M. (2013) In vitro integration of ribosomal RNA synthesis, ribosome assembly, and translation. *Mol. Syst. Biol.*, **9**, 678.
22. Fritz,B.R. and Jewett,M.C. (2014) The impact of transcriptional tuning on in vitro integrated rRNA transcription and ribosome construction. *Nucleic Acids Res.*, **42**, 6774–6785.
23. Liu,Y., Davis,R.G., Thomas,P.M., Kelleher,N.L. and Jewett,M.C. (2021) In vitro-constructed ribosomes enable multi-site incorporation of noncanonical amino acids into proteins. *Biochemistry*, **60**, 161–169.
24. Hammerling,M.J., Fritz,B.R., Yoesep,D.J., Kim,D.S., Carlson,E.D. and Jewett,M.C. (2020) In vitro ribosome synthesis and evolution through ribosome display. *Nat. Commun.*, **11**, 1108.
25. Dohme,F. and Nierhaus,K.H. (1976) Total reconstitution and assembly of 50 S subunits from Escherichia coli Ribosomes in vitro. *J. Mol. Biol.*, **107**, 585–599.
26. Noller,H.F., Kop,J., Wheaton,V., Brosius,J., Gutell,R.R., Kopylov,A.M., Dohme,F., Herr,W., Stahl,D.A., Gupta,R. *et al.* (1981) Secondary structure model for 23S ribosomal RNA. *Nucleic Acids Res.*, **9**, 6167–6189.
27. Nierhaus,K.H. (1990) In: *Ribosomesand protein synthesis: a practical approach*. IRL Pressat Oxford University Press Oxford, Oxford.
28. Russo,C.J. and Passmore,L.A. (2014) Electron microscopy: ultrastable gold substrates for electron cryomicroscopy. *Science*, **346**, 1377–1380.
29. Cheng,A., Negro,C., Bruhn,J.F., Rice,W.J., Dallakyan,S., Eng,E.T., Waterman,D.G., Potter,C.S. and Carragher,B. (2021) Leginon: new features and applications. *Protein Sci.*, **30**, 136–150.
30. Tan,Y.Z., Baldwin,P.R., Davis,J.H., Williamson,J.R., Potter,C.S., Carragher,B. and Lyumkis,D. (2017) Addressing preferred specimen orientation in single-particle cryo-EM through tilting. *Nat. Methods*, **14**, 793–796.
31. Zheng,S.Q., Palovcak,E., Armache,J.P., Verba,K.A., Cheng,Y. and Agard,D.A. (2017) MotionCor2: anisotropic correction of beam-induced motion for improved cryo-electron microscopy. *Nat. Methods*, **14**, 331–332.
32. Lander,G.C., Stagg,S.M., Voss,N.R., Cheng,A., Fellmann,D., Pulokas,J., Yoshioka,C., Irving,C., Mulder,A., Lau,P.W. *et al.* (2009) Appion: an integrated, database-driven pipeline to facilitate EM image processing. *J. Struct. Biol.*, **166**, 95–102.
33. Punjani,A., Rubinstein,J.L., Fleet,D.J. and Brubaker,M.A. (2017) cryoSPARC: algorithms for rapid unsupervised cryo-EM structure determination. *Nat. Methods*, **14**, 290–296.
34. Rohou,A. and Grigorieff,N. (2015) CTFFIND4: fast and accurate defocus estimation from electron micrographs. *J. Struct. Biol.*, **192**, 216–221.
35. Rabuck-Gibbons,J.N., Lyumkis,D. and Williamson,J.R. (2022) Quantitative mining of compositional heterogeneity in cryo-EM datasets of ribosome assembly intermediates. *Structure*, **30**, 498–509.
36. Pettersen,E.F., Goddard,T.D., Huang,C.C., Couch,G.S., Greenblatt,D.M., Meng,E.C. and Ferrin,T.E. (2004) UCSF Chimera – a visualization system for exploratory research and analysis. *J. Comput. Chem.*, **25**, 1605–1612.
37. MacLean,B., Tomazela,D.M., Shulman,N., Chambers,M., Finney,G.L., Frewen,B., Kern,R., Tabb,D.L., Liebler,D.C. and MacCoss,M.J. (2010) Skyline: an open source document editor for creating and analyzing targeted proteomics experiments. *Bioinformatics*, **26**, 966–968.
38. Popova,A.M. and Williamson,J.R. (2014) Quantitative analysis of rRNA modifications using stable isotope labeling and mass spectrometry. *J. Am. Chem. Soc.*, **136**, 2058–2069.
39. Carlile,T.M., Rojas-Duran,M.F. and Gilbert,W.V. (2015) Pseudo-Seq: genome-wide detection of pseudouridine modifications in RNA. *Methods Enzymol.*, **560**, 219–245.
40. Sperling,E., Bunner,A.E., Sykes,M.T. and Williamson,J.R. (2008) Quantitative analysis of isotope distributions in proteomic mass

spectrometry using least-squares Fourier transform convolution. *Anal. Chem.*, **80**, 4906–4917.
41. Liu,Y., Fritz,B.R., Anderson,M.J., Schoborg,J.A. and Jewett,M.C. (2015) Characterizing and alleviating substrate limitations for improved in vitro ribosome construction. *ACS Synth Biol*, **4**, 454–462.
42. Washburn,R.S., Zuber,P.K., Sun,M., Hashem,Y., Shen,B., Li,W., Harvey,S., Acosta Reyes,F.J., Gottesman,M.E., Knauer,S.H. *et al.* (2020) *Escherichia coli* NusG links the lead ribosome with the transcription elongation complex. *Iscience*, **23**, 101352.
43. Huang,Y.H., Hilal,T., Loll,B., Bürger,J., Mielke,T., Böttcher,C., Said,N. and Wahl,M.C. (2020) Structure-based mechanisms of a molecular RNA polymerase/chaperone machine required for ribosome biosynthesis. *Mol. Cell*, **79**, 1024–1036.
44. Lewicki,B.T., Margus,T., Remme,J. and Nierhaus,K.H. (1993) Coupling of rRNA transcription and ribosomal assembly in vivo: Formation of active ribosomal subunits in Escherichia coli requires transcription of rRNA genes by host RNA polymerase which cannot be replaced by bacteriophage T7 RNA polymerase. *J. Mol. Biol.*, **231**, 581–593.
45. Sergiev,P.V., Aleksashin,N.A., Chugunova,A.A., Polikanov,Y.S. and Dontsova,O.A. (2018) Structural and evolutionary insights into ribosomal RNA methylation. *Nat. Chem. Biol.*, **14**, 226–235.
46. Penzo,M. and Montanaro,L. (2018) Turning Uridines around: Role of rRNA Pseudouridylation in Ribosome Biogenesis and Ribosomal Function. *Biomolecules*, **8**, 38.
47. Sergeeva,O.V., Bogdanov,A.A. and Sergiev,P.V. (2015) What do we know about ribosomal RNA methylation in *Escherichia coli*?*Biochimie*, **117**, 110–118.
48. Trubetskoy,D., Proux,F., Allemand,F., Dreyfus,M. and Iost,I. (2009) SrmB, a DEAD-box helicase involved in Escherichia coli ribosome assembly, is specifically targeted to 23S rRNA in vivo. *Nucleic Acids Res.*, **37**, 6540–6549.
49. Oerum,S., Dendooven,T., Catala,M., Gilet,L., Dégut,C., Trinquier,A., Bourguet,M., Barraud,P., Cianferani,S., Luisi,B.F. *et al.* (2020) Structures of *B. subtilis* maturation RNases captured on 50S ribosome with pre-rRNAs. *Mol. Cell*, **80**, 227–236.
50. Spillmann,S., Dohme,F. and Nierhaus,K.H. (1977) Assembly in vitro of the 50 S subunit from Escherichia coli ribosomes: proteins essential for the first heat-dependent conformational change. *J. Mol. Biol.*, **115**, 513–523.
51. Chen,S.S. and Williamson,J.R. (2013) Characterization of the ribosome biogenesis landscape in E. coli using quantitative mass spectrometry. *J. Mol. Biol.*, **425**, 767–779.
52. Geffroy,L., Bizebard,T., Aoyama,R., Ueda,T. and Bockelmann,U. (2019) Force measurements show that uL4 and uL24 mechanically stabilize a fragment of 23S rRNA essential for ribosome assembly. *RNA*, **25**, 472–480.
53. Nowotny,V. and Nierhaus,K.H. (1982) Initiator proteins for the assembly of the 50S subunit from *Escherichia coli* ribosomes. *Proc. Natl. Acad. Sci. U.S.A.*, **79**, 7238–7242.
54. Stelzl,U. and Nierhaus,K.H. (2001) A short fragment of 23S rRNA containing the binding sites for two ribosomal proteins, L24 and L4, is a key element for rRNA folding during early assembly. *RNA*, **7**, 598–609.
55. French,S.L. and Miller,O.L. Jr (1989) Transcription mapping of the *Escherichia coli* chromosome by electron microscopy. *J. Bacteriol.*, **171**, 4207–4216.
56. de Narvaez,C.C. and Schaup,H. (1979) In vivo transcriptionally coupled assembly of *Escherichia coli* ribosomal subunits. *J. Mol. Biol.*, **134**, 1–22.
57. Petrov,A.S., Gulen,B., Norris,A.M., Kovacs,N.A., Bernier,C.R., Lanier,K.A., Fox,G.E., Harvey,S.C., Wartell,R.M., Hud,N.V. *et al.* (2015) History of the ribosome and the origin of translation. *Proc. Natl. Acad. Sci. U.S.A.*, **112**, 15396–15401.
58. Vogel,U. and Jensen,K.F. (1995) Effects of the antiterminator BoxA on transcription elongation kinetics and ppGpp inhibition of transcription elongation in *Escherichia coli*. *J. Biol. Chem.*, **270**, 18335–18340.
59. Vogel,U. and Jensen,K.F. (1994) Effects of guanosine 3 ‘, 5 ‘-bisdiphosphate (ppGpp) on rate of transcription elongation in isoleucine-starved Escherichia coli. *J. Biol. Chem.*, **269**, 16236–16241.
60. Röhl,R. and Nierhaus,K.H. (1982) Assembly map of the large subunit (50S) of *Escherichia coli* ribosomes. *Proc. Natl. Acad. Sci. U.S.A.*, **79**, 729–733.
61. Seffouh,A., Trahan,C., Wasi,T., Jain,N., Basu,K., Britton,R.A., Oeffinger,M. and Ortega,J. (2022) RbgA ensures the correct timing in the maturation of the 50S subunits functional sites. *Nucleic Acids Res.*, **50**, 10801–10816.